

An Integrated Region-, Boundary-, Shape-Based Active Contour for Multiple Object Overlap Resolution in Histological Imagery

Sahirzeeshan Ali* and Anant Madabhushi

Abstract—Active contours and active shape models (ASM) have been widely employed in image segmentation. A major limitation of active contours, however, is in their 1) inability to resolve boundaries of intersecting objects and to 2) handle occlusion. Multiple overlapping objects are typically segmented out as a single object. On the other hand, ASMs are limited by point correspondence issues since object landmarks need to be identified across multiple objects for initial object alignment. ASMs are also constrained in that they can usually only segment a single object in an image. In this paper, we present a novel synergistic boundary and region-based active contour model that incorporates shape priors in a level set formulation with automated initialization based on watershed. We demonstrate an application of these synergistic active contour models using multiple level sets to segment nuclear and glandular structures on digitized histopathology images of breast and prostate biopsy specimens. Unlike previous related approaches, our model is able to resolve object overlap and separate occluded boundaries of multiple objects simultaneously. The energy functional of the active contour is comprised of three terms. The first term is the prior shape term, modeled on the object of interest, thereby constraining the deformation achievable by the active contour. The second term, a boundary-based term detects object boundaries from image gradients. The third term drives the shape prior and the contour towards the object boundary based on region statistics. The results of qualitative and quantitative evaluation on 100 prostate and 14 breast cancer histology images for the task of detecting and segmenting nuclei and lymphocytes reveals that the model easily outperforms two state of the art segmentation schemes (geodesic active contour and Rousson shape-based model) and on average is able to resolve up to 91% of overlapping/occluded structures in the images.

Index Terms—Active contours (ACs), breast, digital pathology, histopathology, hybrid segmentation models, prostate, shape prior, statistical shape models.

I. INTRODUCTION

STATISTICAL shape models (SSMs) [1] and active contours (ACs) have been used widely to segment objects of interest in an array of applications involving biomedical imaging. [2], [3] A fundamental problem when computing SSMs is the determination of correspondences between training instances of the object of interest, especially when the surfaces are represented by point clouds [1]. Often, homologies between the points are assumed, which might lead to an imprecise shape model. A number of active contour segmentation schemes have been developed to date [4]–[9]. They can be divided into two categories: boundary-based and region-based. The boundary-based approaches such as geodesic/geometric active contours have become popular on account of their reliable performance when strong object gradients are present and fast computation [4], [5], [7]. However, as only the edge information is utilized, their performance is limited by the strength of the image gradient. These models are typically unable to handle object occlusion or scene clutter and as a result multiple overlapping objects are often segmented as single object. Region-based approaches rely on statistics obtained from the entire region; color or textural attributes being often employed to detect the object [8]. However, these models typically require far more computations and like the boundary-based approaches are limited in their ability to deal with object occlusions and scene clutter. The integration of prior shape knowledge of the objects for segmentation tasks represents a natural way to solve occlusion problems [9], [10]. Combining a statistical shape prior with geometric/geodesic active contours via a variational model allows for simultaneous registration and segmentation [10]. A limitation of these third generation active contours, however, is that they introduce shape priors into a level set framework in such a way that usually only one pair of overlapping objects can be accurately resolved into independent shapes within an image scene [9], [13].

In the rapidly emerging field of digital pathology, the ability to segment multiple objects, especially the ability to deal with object overlap and occlusion is highly critical in the context of a number of different diagnostic and prognostic applications [2], [16]. Currently, the diagnosis of diseases such as prostate and breast cancer is done manually by visual analysis of tissue samples, typically obtained from a patient via biopsy [6], [15]. The architectural arrangement of nuclear and glandular structures on histopathology is highly relevant in the context of disease grading [6], [14], [15]. Cancer grade in the context of breast

Manuscript received January 22, 2012; accepted February 20, 2012. Date of publication April 05, 2012; date of current version June 26, 2012. This work was supported in part by the W. H. Coulter Foundation, National Cancer Institute (Grant R01CA136535-01, Grant R01CA14077201, Grant, and R03CA143991-01), and in part by The Cancer Institute of New Jersey. *Asterisk indicates corresponding author.*

*S. Ali is with the Department of Electrical and Computer Engineering, Rutgers University, New Brunswick, NJ 08901 USA (e-mail: sahirali@eden.rutgers.edu).

A. Madabhushi is with the Department of Biomedical Engineering, Rutgers University, New Brunswick, NJ 08901 USA (e-mail: anantm@rci.rutgers.edu).

Color versions of one or more of the figures in this paper are available online at <http://ieeexplore.ieee.org>.

Digital Object Identifier 10.1109/TMI.2012.2190089

and prostate cancer is a key feature used to predict patient prognosis and in prescribing a treatment [16]. While grading systems exist in the context of both breast and prostate cancer, manual grading is time consuming and prone to human errors due to observer variability and can lead to variable prognosis and sub-optimal treatment. Automated segmentation and quantification of nuclear and glandular structures is critical for classification and grading of cancer [6], [15]. In the context of prostate cancer (CaP), pathologists grade histopathological specimens by visually characterizing gland morphology and architecture in regions they suspect are malignant. The Gleason grading system is used to describe CaP aggressiveness; lower gleason grade structures such as glands are medium-sized with round shapes, while in higher gleason grade pattern, glands tend to be small and have irregular shapes. Doyle *et al.* [14] showed that spatial graphs (e.g., Voronoi, Delaunay, minimum spanning tree) built using nuclei as vertices in digitized histopathology images, yielded a set of quantitative feature that allowed for improved separation between intermediate gleason patterns. Veltri *et al.* [3] showed that nuclear shape and morphology was reflective of disease aggressiveness and patient outcome. Both of these methods require accurate segmentation of prostate nuclei as an initial step, but had previously employed manual or semi-automated approaches.

Lymphocytic infiltration (LI) has been identified as an important prognostic marker of outcome in Her2+ breast cancer and in other diseases as well [15], [17]. Several researchers for a variety of different diseases have suggested that accurate quantification of lymphocytes could be an important prognostic marker of disease aggressiveness and patient outcome. For instance in the context of ovarian cancer, Asher *et al.* [18] suggested that preoperative platelet lymphocyte ratio was an independent prognostic marker in ovarian cancer. Similarly, Phaloprakarn *et al.* [19] suggested that the ratio of neutrophils to lymphocytes was an important prognostic marker for epithelial ovarian cancer. Similar results have been shown in the context of breast cancers by Martinet *et al.* [20]. Lymphocyte segmentation in hematoxylin and eosin (H&E) stained BC histopathology images is complicated by the similarity in appearance between lymphocytes and other structures (e.g., cancer nuclei) in the image. This may lead to incorrect determination of the extent of LI. Automated detection and quantification of these structures on histopathology imagery could potentially result in the development of a digital prognostic tool for predicting patient outcome (and hence deciding treatment strategies).

However, an automated lymphocyte or nuclear detection algorithm on H&E images has to be able to deal with the 1) variability in digital slide appearance due to inconsistencies in histological staining, 2) poor image quality with tissue samples due to slide digitization, and 3) tissue fixation. Moreover, LI may be characterized by a high density of lymphocytes or nuclei, which could result in images that appear to have significant overlap among lymphocytes and other structures. This often results in adjacent nuclei visually appearing as one single lymphocyte. Basavanthally *et al.* quantified the extent of LI in HER2+ breast cancers using a nuclear detection and graph feature-based approach [15]. Fatakdwal *et al.* [6] combined an expectation maximization scheme with an explicit concavity-

based overlap resolution scheme to separate overlapping lymphocytic nuclei.

In this paper, we present a novel synergistic boundary and region-based active contour model that incorporates shape priors in a level set formulation. We demonstrate an application of these synergistic active contour models using multiple level sets to segment nuclear and glandular structures on digitized histopathology and showcase it's ability in detecting and segmenting all of the overlapping lymphocytes and nuclei simultaneously.

The rest of the paper is structured as follows. Overview of previous related works and novel contributions of this paper in Section II, while shape model formulation is discussed in Section III. Our novel integrated active contour method is presented in Section IV. We describe the experimental design and performance measures in Section V while the analysis of the results is presented in Section VI. In Section VII, we present our concluding remarks and suggest further applications of our scheme.

II. PREVIOUS RELATED WORK AND NOVEL CONTRIBUTIONS

The basic idea behind the AC, as introduced by Kass *et al.* [4], is the following: the segmentation of any object in a given image C , which is well discernible and whose edges can be described by a closed curve, is equivalent to the location of sharp image intensity variations by iteratively deforming a curve C towards the edges of the object. Such a model is entirely dependent on the chosen parametrization of the initial curve $C(p) = (x(p), y(p)) \in \Omega$, $p \in [0, 1]$. Caselles *et al.* [5] proposed to solve the parametrization dependency problem with the geodesic active contour (GAC) model. They introduced a new intrinsic energy functional which is independent of the initial curve parametrization, and minimization of which results in a geodesic in Riemannian space. The associated evolution equation can be written as $\partial_t C = F \cdot \mathcal{N}$ where F is a speed term derived from an energy functional and \mathcal{N} is the exterior unit normal vector to the curve C . To deal with topological changes, the evolution curve is handled by the level set method introduced by Osher and Sethian [21]. The idea is to represent the curve as the level zero of a higher dimensional function ϕ (which is often a signed distance function). This level set function will evolve in time following $\partial_t \phi = F \cdot |\Delta \phi|$ and the interface at the level zero corresponds to the model's evolving contour. AC models [4], [5] based on edge/boundary detection have been previously proposed and these are typically referred to as the first generation of active contours. However, edge-based active contours are very sensitive to noise and require careful initialization. To deal with these problems, segmentation models based on region statistics such as mean, variance, and probability density functions (PDFs) have been developed. Chan and Vese [10] proposed a two-phase segmentation method based on the mean descriptor where the AC evolves in such a way that the difference between the gray level intensity average between the foreground and the background was maximized.

In their seminal work, Cootes *et al.* [1] proposed to use principal component analysis (PCA) to capture the main shape variations of parametric ACs within a training set and thus to represent specific shapes. Consequently, their model is

not parametrization free. Leventon *et al.* [9] proposed the introduction of prior shape information into AC, intrinsically represented by level set functions, the core idea being to apply PCA on the signed distance functions (SDF) of the parametric GACs. This feature allowed them to construct an intrinsic and parametrization free shape model. The shape prior is comprised of the mean level set shape and a weighted sum of the m strongest eigen modes of variation (obtained from the PCA of the SDFs). SDFs have the additional advantage that they are more robust to slight misalignments of the training sequence compared to parametric curves. Unfortunately, the shape functions resulting from PCA are not exactly SDFs, as proved by Leventon *et al.* [9], but they can nonetheless be used in practice since they are very close to real SDFs. Rousson *et al.* [12] proposed a method where the optimal weight factors of the eigenmodes of variation are estimated by solving a linear system. Bresson *et al.* [13] integrated the geometric shape prior of Leventon *et al.* into the segmentation framework based on AC as well as on a region driven term derived from the Chan and Vese energy term [10]. In [11] and [12], the signed distance functions of the training images are computed and the statistics of the signed distance training set is captured via PCA. This representation assumes that the PDF of the training set is Gaussian.

In this work, the contours that segment the object-boundaries are represented using the level set method, and are evolved by minimizing the variational energy. The novel methodological contribution of this work is to learn the shape prior for the target object of interest (nuclei and lymphocytes in our application) and integrate it within a hybrid AC model to segment all the overlapping and nonoverlapping objects within an image simultaneously. Under the level set framework, the contour is represented implicitly as the zero level of a higher dimensional embedding function, and the contour propagation is performed by evolving the embedding function. This enables one to handle topological changes of the boundary such as splitting and merging easily. Unlike previous related work [10], [12], [13], our framework is able to handle simultaneous segmentation of multiple objects. Fig. 1 illustrates the flowchart showcasing our overall segmentation scheme. We present an application of our model for the problem of segmenting multiple, overlapping, and intersecting nuclei and lymphocytes from a total of 114 images from breast and prostate cancer histopathology. The ground truth for quantitative evaluation was provided in the form of nuclear and glandular boundaries by expert pathologists. We anticipate that once tools (such as the one presented in this paper) are made available to the clinical pathologic and biomedical community, prospective clinical trials aimed at explicitly exploring the quantitative, correlative association between nuclear overlap extent and long term patient outcome can be carefully and easily undertaken.

III. SHAPE MODEL FORMULATION

Notation

An image is defined as $\mathcal{C} = (\mathbf{x}, f_g)$ where \mathbf{x} is a 2-D grid representing pixels $c \in \mathbf{x}$, with $c = (x, y)$ representing the Cartesian coordinates of a pixel and f_g assigns intensity values to $c \in \mathbf{x}$, where $f_g(c) \in \mathbb{R}$ (gray scale).

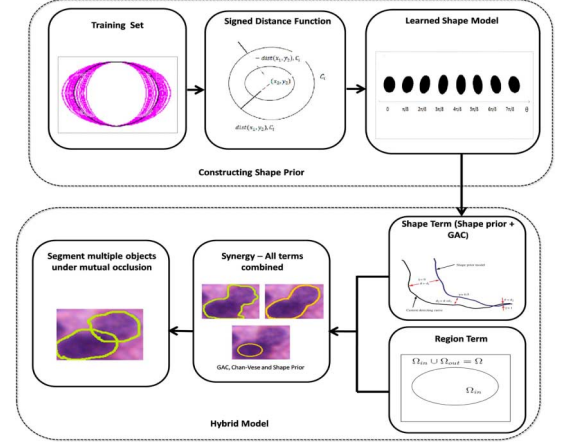


Fig. 1. Flow chart showing the various modules comprising our segmentation scheme. Top row illustrates the construction of shape prior while the bottom row describes the synergy of shape-, region-, and boundary-based terms.

Table I has the description of notations and commonly used symbols in this paper.

A. Shape Alignment

The training shapes are aligned first to the same position, orientation, and scale. The level set functions corresponding to the training shapes are employed for model training. A shape prior model is constructed using statistical methods [9]. In this paper, we only consider objects whose shapes are either view-angle independent or relatively insensitive to view angles. Hence the training shapes are only subject to affine transformations such as translation, rotation and scale. A simple alignment method, the Euclidean similarity transformation (EST) defined as A_s , is adopted for this work. An EST of a point c to a new point c' is defined by the transformation

$$c' = \alpha R c + T \quad (1)$$

where α is the isotropic scaling factor, R is the rotation matrix, and T is the translation vector. For each training shape, the set of parameters (α, R, T) needs to be found to adjust it to the same pose as a predefined (usually arbitrary selected) reference shape. We determine these parameters in the following ways.

- *Translation T* : Obtained by computing the distance between the centroid of target shape (x_i, y_i) and the centroid of reference shape (x_j, y_j)

$$T = \sqrt{(x'_i - x_j)^2 + (y'_i - y_j)^2}. \quad (2)$$

- *Scaling α* : Obtained by computing the ratio of enclosed area of the reference shape ($\mathcal{A}_{\text{reference}}$) over the area of target shape ($\mathcal{A}_{\text{target}}$)

$$\alpha = \frac{|\mathcal{A}_{\text{reference}}|}{|\mathcal{A}_{\text{target}}|} \quad (3)$$

where $|\mathcal{A}|$ represents the cardinality of the set \mathcal{A} . Throughout the whole paper, an image is a 2-D array of pixels, i.e., of unit squares covering a certain area of the real plane in \mathbb{R}^2 . Hence, the number of pixels (cardinality

TABLE I
DESCRIPTION OF NOTATIONS AND COMMONLY USED SYMBOLS IN THIS PAPER

Symbol	Description	Symbol	Description
\mathcal{C}	2D image scene	\mathbf{x}	2D Cartesian grid of pixels $c = (x, y)$
$f_g(c)$	function that assigns intensity values to pixel c	S	the shape contour (zero level set)
\mathbb{C}	the zero level set $\mathbb{C} = \{c \in \Omega : \phi(c) = 0\}$	Ω	bounded open set in \mathbb{R}^2
$H(\phi)$	Heavside function $H(\phi) = \begin{cases} 1, & \phi(c) \geq 0; \\ 0, & \phi(c) < 0. \end{cases}$	$\delta(\phi)$	Delta function $\delta(\phi) = \begin{cases} +\infty, & \phi(c) = 0; \\ 0, & \phi(c) \neq 0. \end{cases}$
Ω_f	foreground region $\Omega_f = \{c \in \Omega : \phi(c) > 0\}$	Ω_b	background region $\Omega_b = \{c \in \Omega : \phi(c) < 0\}$
$\phi(c)$	the level set function	$\mathcal{A}(\cdot)$	the set of pixels within boundary
ψ	the shape function	u_{in}, u_{out}	partitioned foreground and background regions

of the enclosed shape, \mathcal{A}) is directly related to the actual area.

- *Rotation matrix $R(\theta)$* : This is defined as

$$R(\theta) = \begin{bmatrix} \cos(\theta) & -\sin(\theta) \\ \sin(\theta) & \cos(\theta) \end{bmatrix} \quad (4)$$

where θ is an angle between the principal axes of the reference and target shape. Note that this alignment method is also used in adjusting the shape prior model to the same T , R , and α as the shape of the curve undergoing evolution.

B. Creating Training Data

Each aligned shape in the training set is embedded as the zero level set of a higher dimensional surface Υ_e . The points on the surface encode the distance to the nearest point in the shape, with negative distance inside and positive distance outside the shape. The function Υ_e , which is a matrix (or a signed distance map) and of the same size as the training shape template, is defined as

$$\Upsilon_e = \begin{cases} 0, & S \\ -D(c, S), & c \in \Omega_f \\ D(c, S), & c \in \Omega_b \end{cases} \quad (5)$$

where $D(c, S)$ is a function that returns the minimum Euclidean distance between the grid pixel c and the shape contour S , Ω_f is the foreground region, and Ω_b is the background region. To convert these level set functions into feature vectors, they are rearranged into column vectors and form a matrix $M = \{\Upsilon_1, \Upsilon_2, \dots, \Upsilon_n\}$, where M is a $N \times n$ matrix, N is the dimensionality of the feature vectors (SDFs), and n is the number of training samples. On account of the sparseness of the data in the high dimensional space, dimensionality reduction by PCA on the training data, M , is required.

C. Constructing the Shape Prior

Let $\bar{\Upsilon}$ be the mean of training vectors

$$\bar{\Upsilon} = \frac{1}{n} \sum_i \Upsilon_i. \quad (6)$$

Each data is subtracted by the mean vector $\bar{\Upsilon}$ to create the zero-mean vector $\hat{\Upsilon}_i$

$$\hat{\Upsilon}_i = \Upsilon_i - \bar{\Upsilon}. \quad (7)$$

Hence, matrix M becomes \hat{M} . Constructing the covariance matrix C

$$C = \frac{1}{n} \hat{M} \hat{M}^T. \quad (8)$$

Performing the eigen-decomposition on C

$$C = U \Sigma U^T \quad (9)$$

where U is a unitary matrix containing the eigenvectors of C and Σ is the corresponding diagonal matrix of eigenvalues. Matrix U defines a coordinate transform which decorrelates the data and reveals the subspace data resides in. By projecting the data onto the largest h principle components

$$\tilde{\Upsilon}_i = U_h^T (\Upsilon_i - \bar{\Upsilon}) \quad (10)$$

and the dimension of the training data can this be reduced to only h .

Assuming that the feature vectors $\tilde{\Upsilon}$ follow a N dimensional Gaussian distribution, then the probability density function (PDF) associated with the projected data is given as

$$P(\tilde{\Upsilon}) = \frac{1}{(2\pi)^{h/2} |\mathbf{\Lambda}_h|^{1/2}} \exp \left(-\frac{1}{2} \tilde{\Upsilon}^T \mathbf{\Lambda}_h^{-1} \tilde{\Upsilon} \right) \quad (11)$$

where $\tilde{\Upsilon}$ represents projected data from PCA and $\mathbf{\Lambda}_h$ is a diagonal matrix containing the first h eigenvectors. Thus, for a test shape with level set function Υ_t , it's PDF in the subspace is $P(\tilde{\Upsilon}_t)$. Minimizing the PDF in (11) gives us the shape prior ψ . For computational convenience, we compute the negative logarithm of the probability function (ignoring the constant part in (11) in performing the minimization)

$$\begin{aligned} \psi &= -\log[P(\tilde{\Upsilon}_t)] \\ &= \log[(2\pi)^{h/2} |\mathbf{\Lambda}_h|^{1/2}] \\ &\quad + \left[-\frac{1}{2} \tilde{\Upsilon}_t^T \mathbf{\Lambda}_h^{-1} \tilde{\Upsilon}_t \right] \\ &\propto -\frac{1}{2} \tilde{\Upsilon}_t^T \mathbf{\Lambda}_h^{-1} \tilde{\Upsilon}_t. \end{aligned} \quad (12)$$

Minimizing ψ is equivalent to maximizing the PDF. As ψ is a convex function, we search along its gradient descent direction

$$\begin{aligned} [\tilde{\Upsilon}_t]_{n+1} &= [\tilde{\Upsilon}_t]_n - \varepsilon \nabla \psi \\ &= [\tilde{\Upsilon}_t]_n - \varepsilon \mathbf{\Lambda}_h^{-1} [\tilde{\Upsilon}_t]_n. \end{aligned} \quad (13)$$

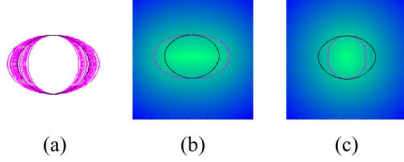


Fig. 2. (a) The set of 30 aligned training ellipses with the mean ellipse shown via a dotted line. Fig. 2(b) and (c) represent $\pm 2\lambda_1$, the unique eigenmode of variation of SDF ellipses whose λ_1 is the eigenvalue.

By iteratively updating $\tilde{\Upsilon}_t$ in (13), the maximum value of $P(\tilde{\Upsilon}_t)$ is found [13]. During each step of the iteration, a shape model $[\Upsilon^*]_n$ is constructed using the largest h principle eigenvectors U_h and the mean of the entire training data $\tilde{\Upsilon}$

$$[\Upsilon^*]_n = U_h[\tilde{\Upsilon}_t]_n + \tilde{\Upsilon}. \quad (14)$$

$[\Upsilon^*]_n$ is a remap of the point $[\tilde{\Upsilon}_t]_n$ from lower dimensional feature subspace to high dimensional data space. It is a reconstructed level set function of the same size as the training shape template, Υ . Although $[\Upsilon^*]_n$ may not be a true distance function due to the information lose during the reconstruction, it generally contains the properties of smoothness, local region correlation, and zero level set consistence with the original shape. Hence, one may assume that $[\Upsilon^*]_n$ is a level set function as justified in [28].

D. Ellipsoidal Shape Prior

In this paper, we chose to model the structures of interest (nuclei, lymphocytes) via 2D ellipses. A number of nuclei were manually delineated from a training set. Major and minor axis of these ellipses was computed. The average major and minor axis were then used to create a mean ellipse model and we created other exemplar ellipses by considering ± 3 standard deviations from the mean. This training data was then used to estimate the mean and standard deviation of the Gaussian function. We generated a training set of 30 ellipses by changing the length of a principle axis with a Gaussian probability function and applied PCA on the SDFs of 30 training ellipses. We extract the one principle component that explains 98% of the variance in the shape of the ellipses and the shape function corresponding to the mean and the eigenmode of variation of the training set [Fig. 2]. Note that, we recognize that the additional PCA step is not necessary with simple ellipses, however, in future we may want to model (a) more complex shapes as shape prior, or (b) may want to explicitly shape such as the scheme used with statistical shape models (ASMs). For these two scenarios PCA is important. With an eye to these possible scenarios we decided to retain the additional PCA step.

IV. INTEGRATED ACTIVE CONTOUR FORMULATION

A. Shape Term

Each shape in the training set is embedded as the zero level set of a higher dimensional surface. A signed distance function (SDF) is used to encode the distance of the shape contour to the nearest point in the shape space. F_{shape} is a functional that depends on the AC providing the boundaries. This functional

evaluates the shape difference between the level set ϕ and the zero level set of the shape prior ψ . It should be noted that PCA applied on aligned SDFs of a training set produces shape functions very close to SDF. The level set formulation of the shape functional is given as

$$F_{\text{shape}} = \int_{\Omega} (\phi(\mathbf{x}) - \psi(\mathbf{x}))^2 |\nabla \phi| \delta(\phi) d\mathbf{x} \quad (15)$$

where ϕ is a level set function and ψ is the shape prior. Since ϕ undergoes a similarity transformation to adjust the pose and scale, we can also write F_{shape} in terms of rotation, translation, and a scaling factor.

The above model introduces the shape prior in such a way that only objects of interest similar to the shape prior can be recovered, and all unfamiliar image structures are suppressed. However, this formulation solves for a single level set consistent with the shape prior. If there are several objects corresponding to the same shape in the scene, this model finds at most *one* object. Often it may not find any matching objects in the scene.

B. Region Homogeneity Term

We define a functional to drive the shape model towards a homogeneous intensity region using the shape prior. If our objects of interest have a smooth intensity surface, then the Mumford–Shah (MS) model is the most appropriate model to segment these objects [8]. Since the MS method applied on the AC will extract globally homogeneous regions and our objective is to capture an object corresponding to a particular shape space, the best solution is to apply the MS-based force on the shape prior [8]. Indeed, this new force will globally drive the shape prior towards a homogeneous intensity region based on the shape of interest. The functional F_{region} can be written with the shape function ψ and statistics of partitioned foreground and background regions, $u_{\text{in}}, u_{\text{out}}$

$$F_{\text{region}}(\psi, u_{\text{in}}, u_{\text{out}}) = \int_{\Omega} \Theta_{\text{in}} H_{\psi} d\mathbf{x} + \int_{\Omega} \Theta_{\text{out}} H_{-\psi} d\mathbf{x} \quad (16)$$

where ψ is the shape function, H_{ψ} is the Heaviside function [8], $\Theta_r = |I - u_r|^2 + \mu |\nabla u_r|^2$ and $r \in \{\text{in}, \text{out}\}$.

C. Combining Shape-, Boundary-, and Region-Based Functionals

We define a synergistic model to address the problem of object segmentation, integrating a geometric shape prior with local and global intensity information within a variational framework

$$F = F_1 + F_{\text{region}}(\psi, u_{\text{in}}, u_{\text{out}}) \quad (17)$$

$$\begin{aligned} F_1 &= \beta_1 F_{\text{shape}}(C) + \beta_2 F_{\text{boundary}}(\phi, \psi) \\ &= \int_{\Omega} \beta_1 ((\phi(\mathbf{x}) - \psi(\mathbf{x}))^2) + \beta_2 (g(|\nabla f_g|) |\nabla \phi| \delta(\phi)) d\mathbf{x} \end{aligned} \quad (18)$$

where ψ is the shape function of the object of interest given by the PCA (see Section III), g is an edge detecting function, $\delta(\cdot)$ is the Dirac delta function, and $\delta(\phi)$ is the contour measure on $\{\phi = 0\}$, and β_1, β_2 are arbitrary positive constants that balance the contributions of the boundary, shape, and region terms. The proposed functional F_1 is an extension of the work of Chen *et*

al. [10] where we have integrated a new statistical shape model. Writing out (17) in its entirety we have

$$\begin{aligned}
 F(\Phi, \Psi, u_{\text{in}}, u_{\text{out}}) &= \underbrace{\int_{\Omega} \beta_1((\phi(\mathbf{x}) - \psi(\mathbf{x}))^2) + \beta_2(g(|\nabla f_g|)|\nabla \phi|\delta(\phi))d\mathbf{x}}_{\text{Shape+boundaryforce}} \\
 &\quad + \underbrace{\beta_r \int_{\Omega} \Theta_{\text{in}} H_{\psi} d\mathbf{x} + \int_{\Omega} \Theta_{\text{out}} H_{-\psi} d\mathbf{x}}_{\text{Regionforce}}. \quad (19)
 \end{aligned}$$

Proof of existence of solution for above model is provided in Appendix B.

D. Segmenting Multiple Objects Under Mutual Occlusion

The level set formulation in (19) is limited in that it allows for segmentation of only a single object at a time. In this work, we incorporate the method presented in [22] into (19). Consider a given image consisting of multiple objects $\{O_1, O_2, \dots, O_m\}$ of the same shape. For the problems considered in this work (nuclei segmentation on histopathology images), all nuclei are assumed to be roughly elliptical in shape. Instead of partitioning the image domain into mutually exclusive regions, we allow each pixel to be associated with multiple objects or the background. Specifically, we try to find a set of characteristic functions χ_f such that

$$\chi_f(\mathbf{x}) = \begin{cases} 1, & \text{if } x \in O_f \\ 0, & \text{if otherwise.} \end{cases} \quad (20)$$

We associate one level set per object in such a way that any $O_k, O_l, k, l \in \{1, 2, \dots, m\}$ are allowed to overlap with each other within the image. These level set components may both be positive within the area of overlap, and enforce the prior on the shapes of objects extracted from the image. We consider a specific case of segmenting two objects within an input image, which is generalizable to N independent familiar objects.

The simultaneous segmentation of two familiar objects with respect to the given shape prior is solved by minimizing the following modified version of (19)

$$\begin{aligned}
 F(\Phi, \Psi, u_{\text{in}}, u_{\text{out}}) &= \sum_{a=1}^2 \int_{\Omega} \beta_1(\phi_a(\mathbf{x}) - \psi(\mathbf{x}))^2 \\
 &\quad + \beta_2(g(|\nabla f_g|)|\nabla \phi_a|\delta(\phi_a))d\mathbf{x} \\
 &\quad + \beta_r \int_{\Omega} (\Theta_{\text{in}} H_{\chi_1 \vee \chi_2}) d\mathbf{x} \\
 &\quad + \int_{\Omega} (\Theta_{\text{out}} - H_{\chi_1 \vee \chi_2}) d\mathbf{x} \\
 &\quad + \omega \int_{\Omega} H_{\chi_1 \wedge \chi_2} d\mathbf{x} + \sum_{a=1}^2 \int_{\Omega} (\phi_a - \psi_a)^2 d\mathbf{x} \quad (21)
 \end{aligned}$$

where $H_{\chi_1 \vee \chi_2} = H_{\psi_1} + H_{\psi_2} - H_{\psi_1} H_{\psi_2}$, $H_{\chi_1 \wedge \chi_2} = H_{\psi_1} H_{\psi_2}$, $\Phi = (\phi_1, \phi_2)$, and $\Psi = (\psi_1, \psi_2)$. The fifth term penalizes the overlapping area between the two regions being segmented, and it prevents the two evolving level set functions from becoming identical. Minimizing (21) by alternating with respect to dynamic variables, yields the associated Euler–Lagrange

equations, parameterizing the decent direction by time $t > 0$ (see Appendix A).

1) *General Case of $N > 2$* : The method described above can be generalized for simultaneous segmentation of $N > 2$ independent objects, all of which can leverage the shape prior ψ_a . Following is the generalized form of (21):

$$\begin{aligned}
 F(\Phi, \Psi, u_{\text{in}}, u_{\text{out}}) &= \sum_{a=1}^N \int_{\Omega} \beta_1(\phi_a(\mathbf{x}) - \psi(\mathbf{x}))^2 \\
 &\quad + \beta_2(g(|\nabla f_g|)|\nabla \phi_a|\delta(\phi_a))d\mathbf{x} \\
 &\quad + \beta_r \int_{\Omega} (\Theta_{\text{in}} H_{\chi_1 \vee \chi_2}) d\mathbf{x} \\
 &\quad + \int_{\Omega} (\Theta_{\text{out}} - H_{\chi_1 \vee \chi_2}) d\mathbf{x} \\
 &\quad + \omega \sum_{a \neq b} \int_{\Omega} H_{\chi_1 \wedge \chi_2} d\mathbf{x} \\
 &\quad + \sum_{a=1}^N \int_{\Omega} (\phi_a - \psi_a)^2 d\mathbf{x}. \quad (22)
 \end{aligned}$$

V. EXPERIMENTAL DESIGN AND PERFORMANCE MEASURES

A. Watershed-Based Initialization of AC Model

To address the issue of model initialization, we propose to use the popular watershed transformation to get the initial delineation and initialize the level sets accordingly. In literature, the watershed transform is often applied to segment touching objects [27]. The watershed transform can be classified as a region-based segmentation approach. The intuitive idea underlying this method comes from geography: it is that of a landscape or topographic relief which is flooded by water, watersheds being the divide lines of the domains of attraction of rain falling over the region [26]. By creating a binary mask of the delineations, we obtain the estimated boundaries of the objects presents.

B. Model Parameters and Data Description

In this paper, for the shape model, we generate a training set of 30 ellipses (nuclei and lymphocytes being elliptical in shape) by changing the size of a principal axis with a gaussian probability function. The manner of choosing the weighting parameters for (17) and (19) is as follows: β_2 is always equal to 1, μ determines the size of the neighborhood where the grey value information is averaged by means of diffusion, β_r is chosen such that the shape prior is attracted towards the region to be segmented, and β_1 is selected in order to allow the active contour to move around the shape prior to capture local boundaries.

Evaluation is done on two different histopathology datasets: breast cancer and prostate cancer cohorts comprising 100 and 14 images respectively (see Table II). A total of 100 cancer nuclei from the images in dataset 1 and 800 lymphocytes from the images in dataset 2 were manually delineated by an expert pathologist (serving as the ground truth annotation for quantitative evaluation). Qualitative evaluation of the model was visually done across all 114 images.

TABLE II
DESCRIPTION OF THE DIFFERENT DATA SETS CONSIDERED IN THIS STUDY

	Name	Number
Dataset 1	H&E stained prostate needle core biopsy images	14
Dataset 2	H&E stained breast biopsy images	100

C. Comparative Strategies and Experiments

We qualitatively and quantitatively compared the segmentation performance of our hybrid AC scheme with the GAC [5] and the Rousson shape-based model (RD) [12]. The RD model is a popular region-based AC model where the model is driven by the Gaussian distribution of both foreground and background and also involves a shape prior.

1) *Experiment 1: Evaluating Overlap Resolution:* The aim of this experiment was to demonstrate the ability of our scheme to correctly resolve the overlap between all intersecting lymphocytes and nuclei across 114 breast and prostate cancer histopathology images.

2) *Experiment 2: Comparing Our Hybrid Model Against the GAC and RD Models in Terms of Detection Accuracy:* The aim of this experiment was to compare the nuclear detection accuracy of our model over two state-of-the-art AC models, GAC and RD.

3) *Experiment 3: Comparing Our Hybrid Model Against GAC and RD Models in Terms of Segmentation Accuracy:* The aim of this experiment was to compare the segmentation performance in terms of boundary and area overlap metrics of our new hybrid model with respect to the GAC and RD models.

D. Performance Measures

1) *Evaluation of Detection Performance:* The measures used to evaluate object detection include: 1) sensitivity (SN); 2) positive predictive value (PPV); and 3) overlap detection ratio (OR) (see Table IV). The detection results from the three models (GAC, our model and RD) are compared to manual detection results obtained via an expert clinician. The SN and PPV values are computed from the true-positive (TP), false-positive (FP), and false-negative (FN) values (TP, FN, FP are subsequently defined)

$$SN = \frac{TP}{TP + FN} \quad (23)$$

$$PPV = \frac{TP}{TP + FP} \quad (24)$$

TP refers to the number of nuclei correctly identified while FP refers to the number of objects incorrectly identified as lymphocytes and FN refers to the number of lymphocytes missed by the model. The detection results are represented as the centroid of the region enclosed by a closed contour. An nuclear object was determined to be a TP if the model detected centroid was found to be within predefined distance (in our case 0.45 mm) of the expert delineated nuclear centroid. Similarly, a FP is identified as an object centroid identified by the model which is greater than predefined distance of a true nuclear centroid. A FN is a true nuclear centroid, for which has no model detected centroid was located within some predefined distance.

2) *Evaluating Overlap Resolution:* The overlap resolution (OR) [6] (Table II) measure is computed as follows:

$$OR = \frac{\text{Number of overlaps resolved}}{\text{Total number of overlaps}}.$$

An overlap is characterized by the existence of a common boundary between two objects and in our case may be between two or more nuclei.

3) *Evaluation of Segmentation Performance:* Segmentation results are compared to manual delineations performed by an expert oncologist (which serves as ground truth for segmentation evaluation) by computing boundary-based metrics, namely Hausdorff distance (HD), mean absolute distance (MAD), and area overlap metrics [true positive area (TP_a), false-positive area (FP_a), true-negative area (TN_a), and false-negative area (FN_a)]. The manual delineation is represented as a closed boundary \mathcal{G} .

Since manual delineation of 100 BC and 14 CaP images is tedious and time consuming, the expert was asked to provide manual delineations of 100 and 800 nuclei randomly chosen from prostate and breast data set, respectively. For each of the object boundary segmentations, a corresponding value for HD and MAD were obtained. HD and MAD values close to zero correspond to better segmentation. The area overlap metrics are used to compute the sensitivity SN_a , specificity SP_a , positive predictive value PPV_a , and the overlap ratio OV_a of the segmentation results for each of the three models. The area overlap metrics are computed as follows:

$$TP_a = \frac{|\mathcal{A}(S) \cap \mathcal{A}(\mathcal{G})|}{\mathcal{A}(\mathcal{G})}$$

$$FP_a = \frac{|\mathcal{A}(S) \cup \mathcal{A}(\mathcal{G}) - \mathcal{A}(\mathcal{G})|}{\mathcal{A}(\mathcal{G})}$$

$$FN_a = \frac{|\mathcal{A}(S) \cup \mathcal{A}(\mathcal{G}) - \mathcal{A}(S)|}{\mathcal{A}(\mathcal{G})}$$

and

$$TN_a = \frac{|\mathbf{C} - \mathcal{A}(\mathcal{G})|}{\mathcal{A}(\mathcal{G})}$$

where $\mathcal{A}(\cdot)$ is the area of the closed boundary. For each image, the set of pixels lying within the manual delineations of the nuclei is denoted as $\mathcal{A}(\mathcal{G})$. $\mathcal{A}(S)$ is the set of pixels whose level set functions are positive, after the convergence of the active contour model. The SN_a and PPV_a values are computed as described in (23) and (24), respectively. SP_a and OV_a values are computed as follows:

$$SP_a = \frac{TN_a}{TN_a + FP_a},$$

$$OV_a = \frac{TP_a}{TP_a + FP_a + FN_a}.$$

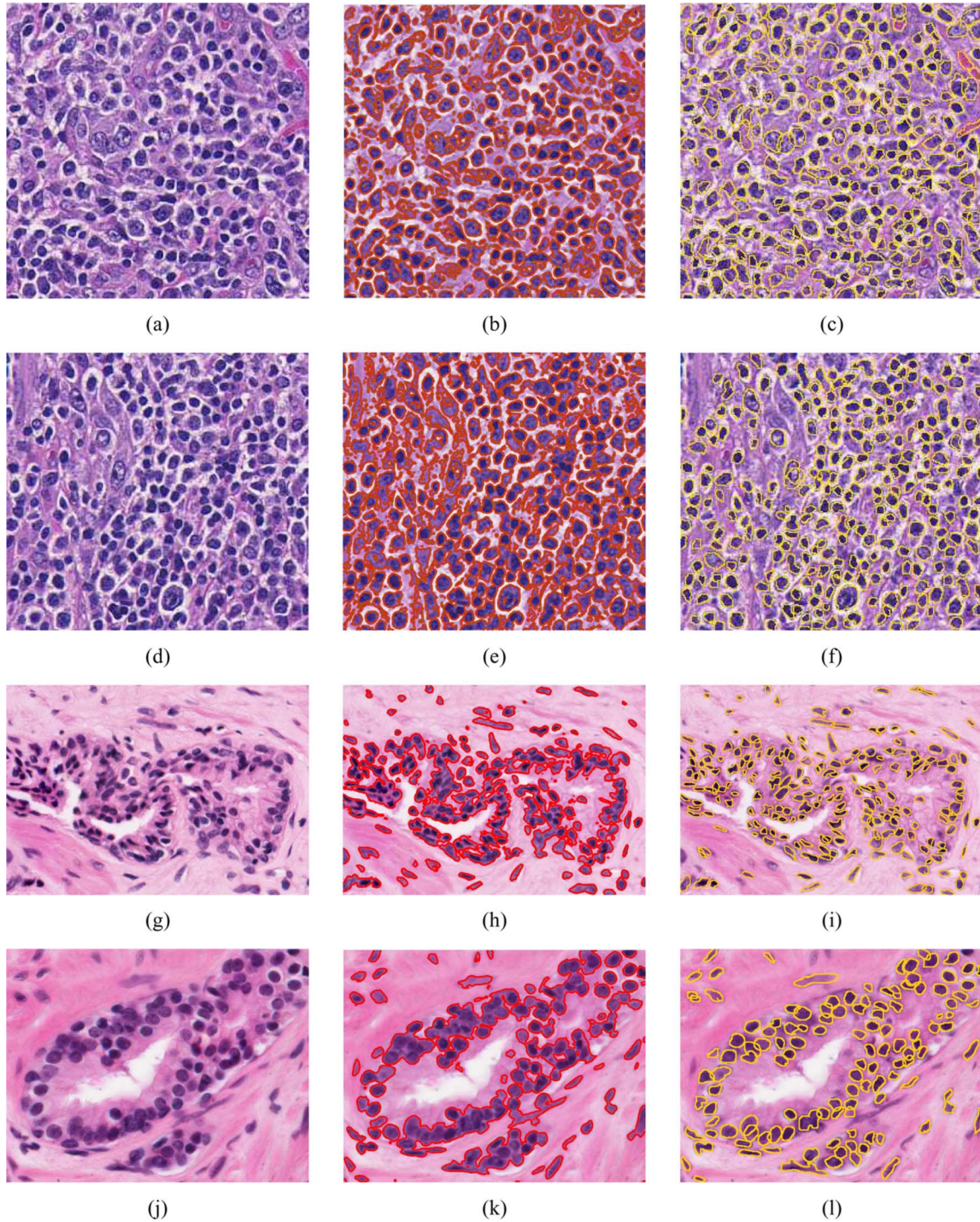


Fig. 3. (a), (d), (g), (j) Original histological image. (b), (e), (h), (k) Segmentation results from GAC Model. (c), (f), (i), (l) Segmentation results from our model. Note that our model is able to better segment intersecting, overlapping nuclei compared to the GAC model. Top two rows represent breast cancer images while bottom two row of images are of prostate cancer.

VI. RESULTS AND DISCUSSION

A. Qualitative Results

Qualitative results for 3 of the 114 different studies are illustrated in Figs. 3 and 4 and reflect the superiority of our model. For the prostate and breast histology images considered in this study, we apply our model for segmenting the gland lumen and lymphocytes, respectively. The results shown in Figs. 3 and 4

for nuclei segmentation aim to demonstrate the strength of our model in terms of detection, segmentation, and overlap resolution. For both the breast and prostate histology images in Fig. 3 (512×512 patches) and Fig. 4 (200×200 patches), respectively, our model was able to detect and segment lymphocytes and cancer nuclei accurately. Fig. 6 demonstrates the robustness of our model as it provides boundaries close to the actual nuclear boundary and the shape constraint prevents spurious edges. It

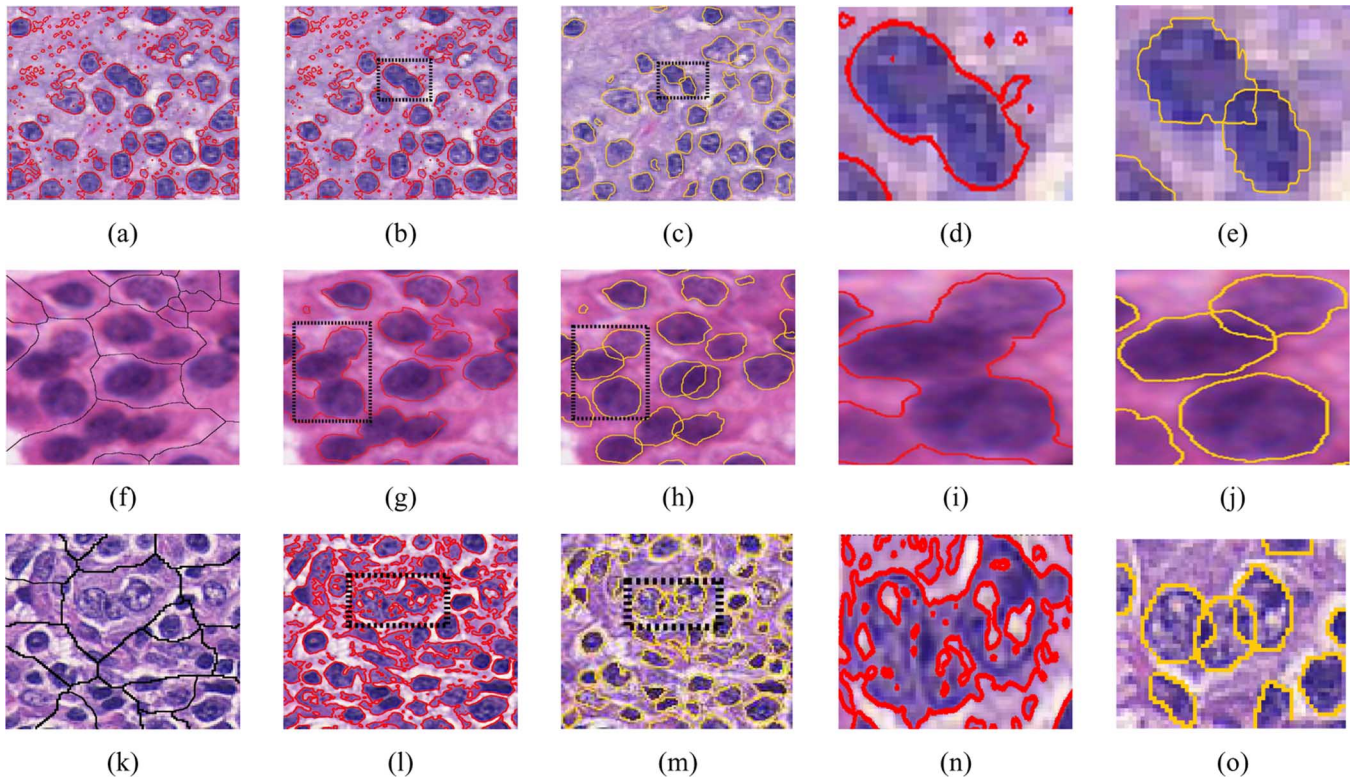


Fig. 4. (a), (f), (k) Watershed initialization of nuclei and lymphocytes on prostate and breast cancer histopathology with corresponding segmentation results obtained via GAC (b), (g), (l); our integrated AC model (c), (h), (m); magnified region (d), (i), (n) from (b), (g), (l); magnified region (e), (j), (o) from (c), (h) and (m).

also demonstrates the ability of our model to segment multiple overlapping objects compared to the RD model.

B. Quantitative Results

Results of quantitative evaluation of detection and segmentation performance for each of the three models are shown in Tables IV–VI. These results reflect the improved performance of our model over RD and GAC models, respectively. The SN and PPV values listed in Tables IV and V reflect the accuracy of our model in detecting lymphocytes in BC images and detecting nuclei in prostate images as compared to the other two models. In terms of segmentation performance, our model easily outperformed the RD and GAC models, in terms of all six segmentation evaluation measures over 800 lymphocytes obtained from 100 breast cancer histopathology images. Fig. 5 shows histogram plots of the HD and MAD values for the three models over 800 lymphocytes from 100 breast histology images for which segmentation evaluation was done. The HD and MAD values for our model were less than five pixels in over 95% and 99% of the cases, respectively. The statistical measures from the area overlap metrics are summarized in Table VI.

A total of 250 cases of overlapping objects were manually identified in 114 images from datasets 1 and 2 (see Table III). Our model was able to resolve 228 (91.2%) overlaps. Tables IV and V contains the summary of detection results for both datasets in terms of SN, PPV, and OR. Results reflect the superiority of our model in terms of detection accuracy compared to the RD and GAC models. OR results as indicated qualitatively in the images and quantitatively in Table V reflect the strength

of our model. The occasional error in resolving overlaps is probably on account of the sensitivity of the active contour to initialization of the level sets (via the watershed scheme).

C. Test of Statistical Significance Between Models

For each of the 114 studies, performance evaluation metrics (SN, PPV, SN_a , PPV_a , SP_a , OV_a , HD, and MAD) were compared for every pair of models (RD-our model, GAC-our model, RD-GAC) using the paired t-test under the null hypothesis that there is no significant difference in the values of the metrics between all three models. The null-hypothesis was rejected for $p\text{-value} \leq 0.05$ (see Table VII). For almost every performance metric (except for two), our model showed a statistically significant improvement compared to GAC and Rousson models.

VII. CONCLUDING REMARKS

We presented a novel segmentation method that uses boundary- and region-based active contours with statistical shape model to accurately detect all the specific shapes in the scene. Furthermore, we presented our model in a multiple level set formulation to segment multiple objects under mutual occlusion. Our test results show that our model is accurate compared to traditional active contours and statistical shape models. Our model was able to segment overlapping lymphocytes and lumen with more than 90% accuracy.

The ability to automatically and accurately segment lymphocytes in BC histopathology images may serve to be useful in studying LI and its relation to BC prognosis [8]. The relationship

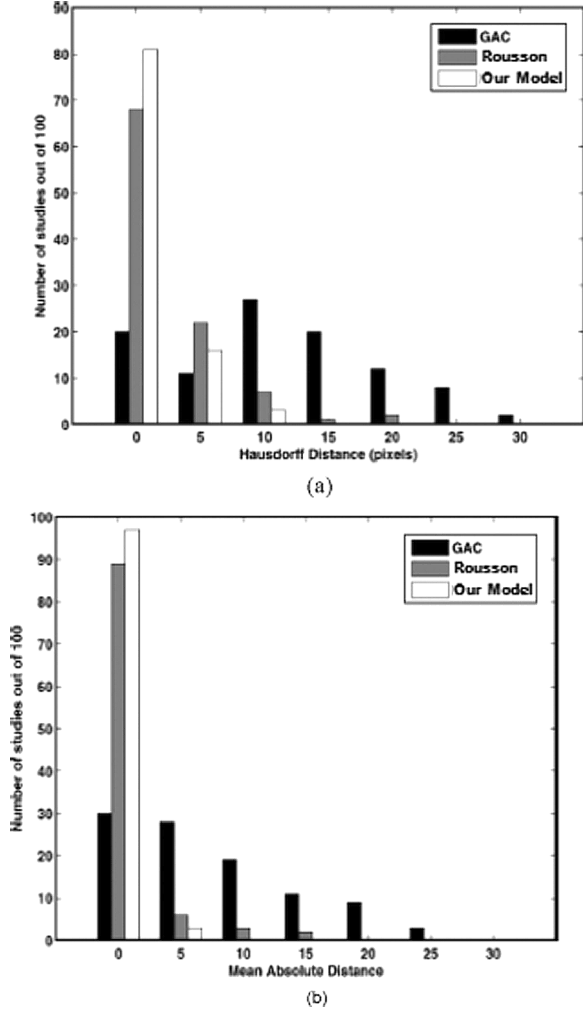


Fig. 5. Histogram for (a) HD and (b) MAD for each of the three models. The plot reflects the number of studies (y -axis) for which the HD and MAD values were below a certain number of image pixels (X -axis).

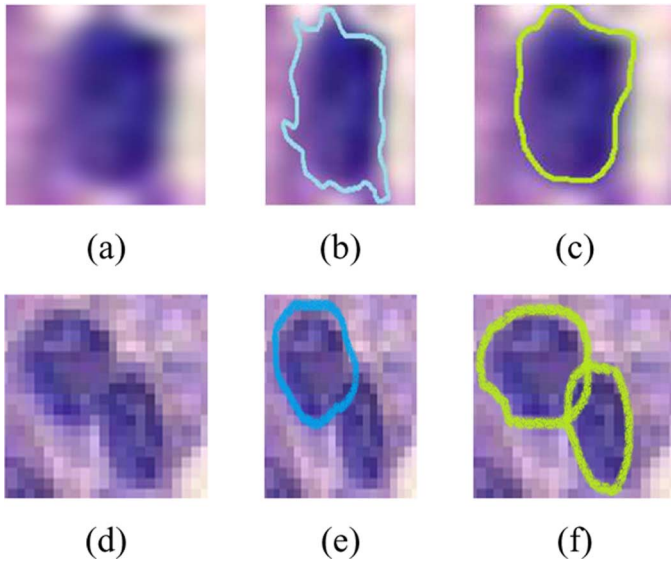


Fig. 6. (a), (d) Original Image. (b), (e) Segmentation given via RD. (c), (f) Segmentation given via our model.

between the presence of LI and good prognosis has also been observed in other pathologies such as ovarian cancer. Hence, the

TABLE III
DESCRIPTION OF THE NUMBER OF STUDIES (DETECTION, SEGMENTATION, AND OVERLAP RESOLUTION) FOR WHICH THIS MODEL WAS EVALUATED

	Dataset 1	Dataset 2
Comparative Strategy	No. of Nuclei	No. of Nuclei
Detection	100	800
Segmentation	100	800
Overlap resolution	50	200

TABLE IV
QUANTITATIVE EVALUATION OF DETECTION RESULTS FOR THE THREE MODELS OVER 100 BREAST HISTOLOGY IMAGES

	SN	PPV	OR
GAC	0.20	0.58	0.022
RD	0.59	0.63	0.74
Our Model	0.86	0.67	0.91

TABLE V
QUANTITATIVE EVALUATION OF DETECTION RESULTS FOR THE THREE MODELS OVER 14 PROSTATE HISTOLOGY IMAGES

	SN	PPV	OR
GAC	0.22	0.55	0.030
RD	0.63	0.63	0.73
Our Model	0.87	0.64	0.90

TABLE VI
QUANTITATIVE EVALUATION OF SEGMENTATION RESULTS BETWEEN GAC, ROUSSON, AND OUR MODEL FOR 800 LYMPHOCYTES

	SN_a	SP_a	PPV_a	OV_a	HD	MAD
GAC	0.31	0.94	0.21	0.17	11.3	7.6
RP	0.81	0.90	0.60	0.49	2.9	1.5
Our model	0.80	1.0	0.86	0.72	2.1	1.1

algorithm developed in this study might also be similarly employed in prognosis prediction of other diseases. Our approach is readily extensible to other objects of interests, such as glandular structures found in prostate and breast cancer.

APPENDIX A

DESCRITIZED ITERATIVE SCHEME: Minimizing (21) iteratively with respect to dynamic variables, yields the associated Euler-Lagrange equations, parameterizing the descent direction, in terms of rotation, scale and translation, by an artificial time $t > 0$ as follows:

$$\begin{aligned}
 \frac{\partial \phi_i}{\partial t} &= \delta_{\phi_i} \left[\mu \nabla \cdot \left(\frac{\nabla \phi}{|\nabla \phi|} \right) \right. \\
 &\quad \left. - (((f - u_{in})^2 + (f - u_{out})^2)(1 - H_{\phi_j})) \right] \\
 &\quad - 2v(\phi_i - \psi_i) \\
 \frac{\partial \theta_i}{\partial t} &= 2v \int_{\Omega} (\phi_i - \psi_i)(\nabla \psi_i \cdot \nabla_{\Theta} A_i) dx \\
 \frac{\partial T_i}{\partial t} &= 2v \int_{\Omega} (\phi_i - \psi_i)(\nabla \psi_i \cdot \nabla_T A_i) dx \\
 \frac{\partial \alpha_i}{\partial t} &= 2v \int_{\Omega} (\phi_i - \psi_i) \left(-\frac{\psi_i}{s} + \nabla \psi_i \cdot \nabla_{\alpha} A_i \right) dx \\
 &\quad i, j \in \{1, 2\}, i \neq j
 \end{aligned} \tag{25}$$

TABLE VII
P-VALUES OF T-TEST BETWEEN THREE MODELS FOR PERFORMANCE METRICS FROM 114 STUDIES

	SN	PPV	OR	SN_a	SP_a	PPV_a	OV_a	HD	MAD
GAC/Rousson	2.6×10^{-34}	6.1×10^{-3}	1.8×10^{-14}	1.1×10^{-16}	8.1×10^{-3}	1.9×10^{-15}	1.9×10^{-17}	4.5×10^{-16}	1.5×10^{-13}
GAC/Our Model	1.3×10^{-73}	1.4×10^{-3}	1.3×10^{-81}	6.1×10^{-18}	8.2×10^{-4}	2.8×10^{-33}	1.2×10^{-31}	3.8×10^{-21}	2.1×10^{-17}
Rousson/Our Model	1.5×10^{-50}	6.9×10^{-1}	1.4×10^{-57}	9.5×10^{-1}	1.3×10^{-4}	7.9×10^{-12}	1.7×10^{-10}	4.6×10^{-3}	1.7×10^{-2}

Similar to Chan–Vese model, we update u_{in} and u_{out} for each iterations as follows:

$$\begin{aligned} u_{in} &= \frac{\int_{\Omega} f H_{\chi_1 \vee \chi_2} dx}{\int_{\Omega} H_{\chi_1 \vee \chi_2} dx} \\ u_{out} &= \frac{\int_{\Omega} f (1 - H_{\chi_1 \vee \chi_2}) dx}{\int_{\Omega} (1 - H_{\chi_1 \vee \chi_2}) dx}. \end{aligned} \quad (26)$$

The above model can be adapted for N objects. To be able to actually solve the equations in (26), we need to discretize it. We do this on a regular 2-D M -by- N grid. We let ℓ denote the spacing between the cells and $(x_i, y_j) = (i\ell, j\ell)$ be the grid points with $0 \leq i \leq M$ and $0 \leq j \leq N$. Discretizing u_{in} and u_{out} is easy, so long as we fix a regularized Heaviside function. For our discretization we have chosen

$$H(z) = \begin{cases} 1, & \text{if } z > \epsilon \\ 0, & \text{if } z < -\epsilon \\ \frac{1}{2} + \frac{z}{2\epsilon} + \frac{1}{2\pi} \sin\left(\frac{\pi z}{\epsilon}\right), & \text{if } |z| \leq \epsilon. \end{cases} \quad (27)$$

To discretize $\nabla \cdot (\nabla \Theta / |\nabla \Theta|)$, that is, the divergence of the normalized gradient of ϕ , we let ϕ_x, ϕ_y denote partial derivatives of ϕ and similarly let ϕ_{xx}, ϕ_{yy} and ϕ_{xy} denote the second-order partial derivatives. Thus, we obtain

$$\nabla \cdot \frac{\nabla \Theta}{|\nabla \Theta|} = \frac{\phi_{xx}\phi_y^2 - 2\phi_{xy}\phi_x\phi_y + \phi_{yy}\phi_x^2}{(\phi_x + \phi_y)^{3/2}} \quad (28)$$

which we discretize with the following approximations using central differences scheme:

$$\begin{aligned} \phi_x(i, j) &= \frac{(x_{i-1}, x_j) - (x_{i+1}, x_j)}{2\ell} \\ \phi_y(i, j) &= \frac{(x_i, x_{j-1}) - (x_i, x_{j+1})}{2\ell} \\ \phi_{xx}(i, j) &= \frac{(x_{i-1}, x_j) - (x_{i+1}, x_j) + 2(x_i, x_j)}{\ell^2} \\ \phi_{yy}(i, j) &= \frac{(x_i, x_{j-1}) - (x_i, x_{j+1}) + 2(x_i, x_j)}{\ell^2} \\ \phi_{xy}(i, j) &= \frac{1}{4\ell^2} \left((x_{i+1}, x_{j+1}) + (x_{i-1}, x_{j+1}) \right. \\ &\quad \left. + (x_{i+1}, x_{j-1}) + (x_{i-1}, x_{j-1}) \right) \end{aligned} \quad (29)$$

APPENDIX B

EXISTENCE OF SOLUTION FOR OUR MINIMIZATION PROBLEM: This section deals with mathematical study of

$$\begin{aligned} \min_{\psi, u_{in}, u_{out}} \left\{ F &= \int_{\Omega} (\phi(\mathbf{x}) - \psi(\mathbf{x}))^2 |\nabla \phi| \delta(\phi) d\mathbf{x} \right. \\ &\quad \left. + \beta_r \int_{\Omega} \left(\Theta_{in} H_{\psi} + \int_{\Omega} \Theta_{out} H_{-\psi} \right) d\mathbf{x} \right\}. \end{aligned} \quad (30)$$

We follow the proofs of Chen *et al.* [23] and Chan *et al.* [8] to prove the existence of a minimizer for our proposed minimization problem using the direct method of the calculus of variations and compactness theorems on the space of functions with bounded variation.

The minimization problem is considered among characteristic functions χ_E of sets $E = \{\mathbf{x} \in \Omega | \phi(\mathbf{x}) \geq 0\}$. This minimization is over all χ_E in $BV(\Omega)$. The vector of PCA eigen-coefficients $x_{pca} = (x_{pca_1}, \dots, x_{pca_h})$ is defined on $\Omega_{pca} = [-3\lambda_1, 3\lambda_1] \times \dots \times [-3\lambda_h, 3\lambda_h]$. Functions u_{in} and u_{out} from Section III-C are supposed in $C^1(\Omega)$. The minimization problem involves a weighted total variation norm for the functions with finite perimeters. It also minimizes more than one argument. To study the existence for the problem (30), it is necessary to introduce the concept of weighted total variation norms for functions of bounded variation. We also remind some definitions and theorems introduced by Evans *et al.* [32], Crandall *et al.* [28], Chen *et al.* [23], Chan *et al.* [8], and Ambrosio *et al.* [30].

Definition 1: Let $\Omega \subset \mathbf{R}^N$ be an open set and let $f \in L^1(\Omega)$. The total variation norm of f is defined by

$$TV(f) = \int_{\Omega} |\nabla f| = \sup_{\phi \in \Phi} \int_{\Omega} f(x) \operatorname{div} \phi(x) \quad (31)$$

where

$$\Phi = \{\phi \in C_0^1(\Omega, \mathbf{R}^N) | \phi(x)| \leq 1, \text{ on } \Omega\}. \quad (32)$$

Definition 2: A function $f \in L^1(\Omega)$ is said to have bounded variation in Ω if its distributional derivative satisfies $TV(f) < \infty$. We define $BV(\Omega)$ as the space of all functions in $L^1(\Omega)$ with bounded variation and endowed with the norm

$$\|f\|_{BV(\Omega)} = \|f\|_{L^1(\Omega)} + TV(f) \quad (33)$$

Hence, $BV(\Omega)$ is a Banach space.

Theorem 1: A measurable subset of E of \mathbf{R}^N has finite perimeter (per_{Ω}) in Ω if and only if the characteristic function $\chi_E \in BV(\Omega)$. We have $per_{\Omega} = TV(\chi_E) = \int_{\Omega} |\nabla \chi_E| < \infty$.

Definition 3: Let $\Omega \subset \mathbf{R}^N$ be an open set and let $f \in L^1(\Omega)$ and $\varphi(x)$ be positive valued continuous and bounded functions on Ω . The weighted total variation norm (TV_{φ}) of f is defined by

$$TV_{\varphi}(f) = \int_{\Omega} \varphi(x) |\nabla f| = \sup_{\phi \in \Phi_{\varphi}} \int_{\Omega} f(x) \operatorname{div} \phi(x) \quad (34)$$

where

$$\Phi_{\varphi} = \{\phi \in C_0^1(\Omega, \mathbf{R}^N) | \phi(x)| \leq \varphi(x), \text{ on } \Omega\}. \quad (35)$$

If a function f has a finite weighted total variation norm in Ω then it also belongs to $BV(\Omega)$.

Definition 4: A function $f \in BV(\Omega)$ is a special function of bounded variation if its distributional derivative is given by

$$|Df| = TV(f) + \int_{\Omega \cap S_f} J_f d\mathcal{H}^{N-1} \quad (36)$$

where J_f is the jump part defined on the set of points S_f and \mathcal{H}^{N-1} is the $(N-1)$ -dimensional Hausdorff measure [31]. The space of special functions of bounded variation $SBV(\Omega)$ is a Banach space, endowed with the norm

$$\|f\|_{SBV(\Omega)} = \|f\|_{L^1(\Omega)} + |Df|. \quad (37)$$

Theorem 2: Let $\Omega \subset \mathbf{R}^N$ be an open set with a lipschitz boundary. If $\{f_n\}_{n \geq 1}$ is a bounded sequence in $BV(\Omega)$, then there exist a subsequence $\{f_{n_j}\}$ of $\{f_n\}$ and a function $f \in BV(\Omega)$, such that $f_{n_j} \rightarrow f$ strongly in $L^p(\Omega)$ for any $1 \leq p < N/N-1$ and

$$TV(f) \leq \liminf_{f_{n_j} \rightarrow \infty} TV(f_{n_j}). \quad (38)$$

The following theorem is a generalization of the main theorem in Chen *et al.* [23].

Theorem 3: Let $\Omega \subset \mathbf{R}^N$ be an open set with a lipschitz boundary. If $\{f_n\}_{n \geq 1}$ is a bounded sequence in $BV(\Omega)$, and if $\{f_n\}_{n \geq 1}$ is a positive valued continuous functions that uniformly converges to α on Ω , then there exist a subsequence $\{f_{n_j}\}$ of $\{f_n\}$ and a function $f \in BV(\Omega)$, such that $f_{n_j} \rightarrow f$ strongly in $L^p(\Omega)$ for any $1 \leq p < N/N-1$ and

$$TV_\varphi(f) \leq \liminf_{f_{n_j} \rightarrow \infty} TV_\varphi(f_{n_j}). \quad (39)$$

Theorem 4: Let Ω be a bounded and open subset of \mathbf{R}^2 and \mathcal{C} be a given image with $\mathcal{C} \in AL^\infty(\Omega)$. The minimization problem may be rewritten in the following form:

$$\min_{\alpha, u_{in}, u_{out}} \left\{ F = \int_{\Omega} (\phi(\mathbf{x}) - \psi(\mathbf{x}))^2 + g(\mathbf{x}) |\nabla \chi_E| + \beta_r F_{\text{region}}(u_{in}, u_{out}, \psi) \right\} \quad (40)$$

has a solution $\chi_E \in BV(\Omega)$, $x_{\text{pca}} \in \Omega_{\text{pca}}$, $u_{in}, u_{out} \in C^1(\Omega)$.

Proof: We use the direct method of the calculus of variations.

- Let $\{\chi_E, x_{\text{pca}}, u_{in}, u_{out}\}$ be a minimizing sequence of (40), i.e.,

$$\lim_{n \rightarrow \infty} F(\chi_{E_n}, x_{\text{pca}_n}, u_{in_n}, u_{out_n}) = \inf_{\chi_E, x_{\text{pca}}, u_{in}, u_{out}} F(\chi_E, x_{\text{pca}}, u_{in}, u_{out}). \quad (41)$$

- Since χ_{E_n} is a sequence of characteristic functions E_n , then $\chi_{E_n}(\mathbf{x}) \in \{0, 1\}$ —a.e. in Ω . A constant $M > 0$ exists such that $\|\nabla \chi_{E_n}\|_{L^1(\Omega)} \leq M, \forall n \geq 1$. Therefore, χ_{E_n} is a uniformly bounded sequence on $BV(\Omega)$.

Since $\{x_{\text{pca}_n}\}$ are bounded sequences on compact space Ω_{pca} , a subsequence $\{x_{\text{pca}_{n_j}}\}$ that converge to limit x_{pca} exists.

The integrand $(\phi(\mathbf{x}) - \psi(\mathbf{x}))^2 + g(\mathbf{x})$ is positive and bounded because both functions are bounded on Ω . Since PCA is applied on continuous functions (SDFs), the

shape prior is also continuous and converges uniformly on Ω . Following theorem 3, a subsequence of χ_{E_n} that converges to a function χ_E strongly in $L^1(\Omega)$ exists. Moreover, Theorem 3 also state that

$$\int_{\Omega} f |\nabla \chi_E| \leq \liminf_{n_j \rightarrow \infty} \int_{\Omega} f_{n_j} |\nabla \chi_{E_{n_j}}|. \quad (42)$$

- In the region-based functional defined in (16)

$$F_{\text{region}}(\psi, u_{in}, u_{out}) = \int_{\Omega} \Theta_{in} H_{\psi} d\mathbf{x} + \int_{\Omega} \Theta_{out} H_{-\psi} d\mathbf{x}, \quad (43)$$

the function H_{ψ} is a characteristic function χ_G of sets $G = \mathbf{x} \in \Omega | \psi(\mathbf{x}) \geq 0$. So we have

$$\int_{\Omega} \Theta_{in} \chi_G d\mathbf{x} + \int_{\Omega} \Theta_{out} (1 - \chi_G) d\mathbf{x} \quad (44)$$

and we can define the function $u = u_{in} \chi_G + u_{out} (1 - \chi_G)$. The minimization sequence of (40) implies

$$\lim_{n \rightarrow \infty} F_{\text{region}}(x_{\text{pca}_n}, u_{in_n}, u_{out_n}) = \inf_{x_{\text{pca}}, u_{in}, u_{out}} F_{\text{region}}(x_{\text{pca}}, u_{in}, u_{out}). \quad (45)$$

Since the function χ_G depends continuously on variable x_{pca} and transformations A_s , we have $\chi_G(\psi) = \chi_{G_n}$ and $u_n = u_{in_n} \chi_{G_n} + u_{out_n} (1 - \chi_{G_n})$. According to Ambrosio's lemma [30], we can deduce that there is a $u \in SBV(\Omega)$, such that a subsequence u_{n_j} converges to u a.e. in BV and

$$F_{\text{region}}(x_{\text{pca}_n}, u_{in_n}, u_{out_n}) = F_{\text{region}}(u) \leq \liminf_{n_j \rightarrow \infty} F_{\text{region}}(u_{n_j}). \quad (46)$$

which means that u is a minimizer of F_{region} . Then, by combining (42) and (46), $\chi_E, x_{\text{pca}}, u_{in}$ and u_{out} are minimizers of (40).

ACKNOWLEDGMENT

The authors would like to thank Dr. J. E. Tomaszewski and Dr. M. D. Feldman from the Pathology Department at the Hospital of the University of Pennsylvania and Dr. S. Ganesan at the Cancer Institute of New Jersey for providing the histology imagery and ground truth annotation.

REFERENCES

- [1] T. F. Cootes, D. Cooper, C. J. Taylor, and J. Graham, "Active shape models—Their training and application," *Comput. Vis. Image Understand.*, vol. 61, no. 1, pp. 38–59, Jan. 1995.
- [2] A. Madabhushi, "Digital pathology image analysis: Opportunities and challenges (editorial)," *Imag. Med.*, vol. 1, no. 1, pp. 7–10, 2009.
- [3] R. W. Veltri, S. Isharwal, and M. C. Mille, "Nuclear roundness variance predicts prostate cancer progression, Metastasis, and death: A prospective evaluation with up to 25 years of follow-up after radical prostatectomy," *Prostate*, vol. 70, pp. 133m–1339, 2010.
- [4] M. Kass, A. Witkin, and D. Terzopoulos, "Snakes: Active contour models," *Int. J. Comput. Vis.*, pp. 321–331, 1987.
- [5] V. Caselles, R. Kimmel, and G. Sapiro, "Geodesic active contours," *Int. J. Comput. Vis.*, vol. 22, no. 1, pp. 61–79, 1997.
- [6] H. Fatakdawala, J. Xu, A. Basavanahally, G. Bhanot, S. Ganesan, M. Feldman, J. Tomaszewski, and A. Madabhushi, "Expectation maximization driven geodesic active contour with overlap resolution (EMaGACOR): Application to lymphocyte segmentation on breast cancer histopathology," *IEEE Trans. Biomed. Eng.*, vol. 57, no. 7, pp. 1676–1689, Jul. 2010.

- [7] S. Kichenassamy, A. Kumar, P. Olver, A. Tann, and A. J. Yezzi, "Conformal curvature flows: From phase transitions to active vision," *Arch. Rational Mech. Anal.*, vol. 134, pp. 275–301, 1996.
- [8] T. F. Chan and L. A. Vese, "Active contours without edges," *IEEE Trans. Image Process.*, vol. 10, no. 2, pp. 266–277, 2001.
- [9] W. Fang and K. L. Chan, "Statistical shape influence in geodesic active contours," in *IEEE Conf. Comput. Vis. Pattern*, 2007, vol. 40, pp. 2163–2172.
- [10] T. Chan, "Level set based shape prior segmentation," in *IEEE Comput. Soc. Conf. Comput. Vis. Pattern Recognit.*, 2005, vol. 2, pp. 1164–1170.
- [11] N. Paragios and R. Deriche, "Unifying boundary and region-based information for geodesic active tracking," in *IEEE Conf. Comput. Vis. Pattern Recognit.*, 1999, vol. 2, pp. 300–305.
- [12] M. Rousson and N. Paragios, "Shape priors for level set representation," in *Eur. Conf. Comput. Vis.*, 2002, pp. 78–92.
- [13] X. Bresson, P. Vanderghenst, and J. P. Thiran, "A priori information in image segmentation: Energy functional based on shape statistical model and image information," in *IEEE Int. Conf. Image Process.*, Sep. 2003, vol. 3, pp. 425–428.
- [14] S. Doyle, M. Hwang, K. Shah, A. Madabhushi, J. Tomaszewski, and M. Feldman, "Automated grading of prostate cancer using architectural and textural image features," in *Proc. Int. Symp. Biomed. Imag. (ISBI)*, 2007, pp. 1284–1287.
- [15] A. Basavanthally, S. Ganesan, S. Agner, J. Monaco, M. Feldman, J. Tomaszewski, G. Bhanot, and A. Madabhushi, "Computerized image-based detection and grading of lymphocytic infiltration in HER2+ Breast cancer histopathology," *IEEE Trans. Biomed. Eng.*, vol. 57, no. 3, pp. 642–653, Mar. 2010.
- [16] M. Gurcan, L. Boucheron, A. Can, A. Madabhushi, N. Rajpoot, and B. Yener, "Histopathological image analysis: A review," *IEEE Rev. Biomed. Eng.*, vol. 2, pp. 147–171, 2009.
- [17] G. Coukos, "Intratumoral T cells, recurrence, and survival in epithelial ovarian cancer," *N. Eng. J. Med.*, 2003.
- [18] V. Asher, J. Lee, A. Innamaa, and A. Bali, "Preoperative platelet lymphocyte ratio as an independent prognostic marker in ovarian cancer," *Clin. Trans. Oncol.*, vol. 13, no. 7, pp. 499–503, Jul. 2011.
- [19] T. Thavaramara, C. Phaloprakarn, S. Tangitgamol, and S. Manusirivithaya, "Role of neutrophil to lymphocyte ratio as a prognostic indicator for epithelial ovarian cancer," *J. Med. Assoc. Thai*, vol. 94, no. 7, pp. 871–877, Jul. 2011.
- [20] L. Martinet, I. Garrido, T. Filleron, S. Le Guellec, E. Bellard, J. J. Fournie, P. Rochaix, and J. P. Girard, "Human solid tumors contain high endothelial venules: Association with T- and B-lymphocyte infiltration and favorable prognosis in breast cancer," *Cancer Res.*, vol. 71, no. 17, pp. 5678–5687, Sep. 2011.
- [21] S. Osher and J. A. Sethian, "Fronts propagating with curvature-dependent speed: Algorithms based on hamilton-jacobi formulations," *J. Computat. Phys.*, vol. 79, no. 1, pp. 12–49, 1988.
- [22] Q. Zhang and R. Pless, "Segmenting multiple familiar objects under mutual occlusion," *ICIP*, 2006.
- [23] Y. Chen, H. D. Tagare, S. Thiruvankadam, F. Huang, D. Wilson, K. S. Gopinath, R. Briggs, W. Richard, and E. A. Geiser, "Using prior shapes in geometric active contours in a variational framework," *Int. J. Comput. Vis.*, vol. 50, no. 3, pp. 315–328, 2002.
- [24] D. Cremers, F. Tischh, Florian, J. Weickert, and C. Schn, "Diffusion snakes: Introducing statistical shape knowledge into the muford-shah functional," *Int. J. Comput. Vis.*, vol. 50, no. 3, pp. 295–313, 2002.
- [25] N. Paragios, M. Rousson, and V. Ramesh, "Matching distance functions: A shape-to-area variational approach for global-to- local registration," in *Proc. Eur. Conf. Comput. Vis.*, 2002, pp. 775–789.
- [26] S. Beucher and F. Meyer, "The morphological approach to segmentation: The watershed transformation," *Math. Morphol. Image Process.*, pp. 433–481, 1993.
- [27] Y. Wenzhong and F. Xiaohui, "A watershed based segmentation method for overlapping chromosome images," in *Proc. 2nd Int. Workshop Edu. Technol. Comput. Sci.*, 2010, vol. 1, pp. 571–573.
- [28] M. G. Crandall, H. Ishii, and P.-L. Linons, "Users guide to viscosity solutions of second order partial differential equations," *Am. Math. Soc. Bull.*, vol. 27, pp. 167–167, 1992.
- [29] G. Dal Maso, J. M. Morel, and S. Solimini, "A variational method in image segmentation: Existence and approximation results," *Acta Mathematica*, vol. 168, pp. 89–151, 1992.
- [30] E. De Giorgi and L. Ambrosio, "New functionals in the calculus of variations," *Atti. Accad. Naz. Lincei Rend. Cl. Sci. Fis. Mat. Natur.*, vol. 82, no. 2, pp. 199–210, 1998.
- [31] E. De Giorgi, M. Carriero, and A. Leaci, "Existence theorem for a minimum problem with free discontinuity set," *Arch. Rational Mech. Anal.*, vol. 108, no. 3, pp. 195–218, 1989.
- [32] L. Evans and R. F. Gariepy, *Measure Theory and Fine Properties of Functions*. Boca Raton, FL: CRC, 1992.